Origin of the magnetostructural coupling in $FeMnP_{0.75}Si_{0.25}$

E. K. Delczeg-Czirjak,[1,*] M. Pereiro,[1] L. Bergqvist,[2] Y. O. Kvashnin,[1] I. Di Marco,[1] Guijiang Li,[3] L. Vitos,[1,3,4] and O. Eriksson[1]

[1]*Division of Materials Theory, Department of Physics and Astronomy, Uppsala University, Box 516, SE-751 20, Uppsala, Sweden*

[2]*Department of Materials and Nano Physics and Swedish e-Science Research Centre, Royal Institute of Technology (KTH), Electrum 229, SE-164 40 Kista, Sweden*

[3]*Applied Materials Physics, Department of Materials Science and Engineering, Royal Institute of Technology (KTH), SE-100 44 Stockholm, Sweden*

[4]*Research Institute for Solid State Physics and Optics, Wigner Research Center for Physics, P.O. Box 49, HU-1525 Budapest, Hungary*

(Received 28 May 2014; revised manuscript received 28 October 2014; published 23 December 2014)

The strong coupling between the crystal structure and magnetic state (ferromagnetic or helical antiferromagnetic) of $FeMnP_{0.75}Si_{0.25}$ is investigated using density functional theory in combination with atomistic spin dynamics. We find many competing energy minima for drastically different ferromagnetic and noncollinear magnetic configurations. We also find that the appearance of a helical spin-spiral magnetic structure at finite temperature is strongly related to one of the crystal structures reported for this material. Shorter Fe-Fe distances are found to lead to a destabilized ferromagnetic coupling, while out-of-plane Mn-Mn exchange interactions become negative with the shortening of the interatomic distances along the *c* axis, implying an antiferromagnetic coupling for the nearest-neighbor Mn-Mn interactions. The impact of the local dynamical correlations is also discussed.

DOI: 10.1103/PhysRevB.90.214436 PACS number(s): 75.30.Sg, 75.50.Ee, 75.40.Gb

I. INTRODUCTION

Magnetocaloric (MC) research has been primarily focused on the ferromagnetic (FM) to paramagnetic (PM) phase transition [1–10]. Promising new directions toward finding well-performing MC materials are those focusing on materials with an antiferromagnetic (AFM) to FM metamagnetic phase transition [11–16]. Widely investigated representatives of this class of materials are the doped MnP-related *Pnma* compounds [13,14]. The strong connection between the magnetic properties and the crystal structure was observed recently for Co- and Ge-doped MnP compounds [17,18]. The magnetic state of these alloys is found to be strongly dependent on the nearest-neighbor (NN) Mn-Mn separation. CoMnP and CoMnGe are collinear ferromagnets, whereas $CoMnP_{1-x}Ge_x$ ($x \approx 0.5$) has an AFM ground state. The shortest Mn-Mn distance has an intermediate value for $CoMnP_{1-x}Ge_x$, while CoMnP possesses the shortest NN distance and CoMnGe has the largest Mn-Mn NN distance. The coupling between the type of magnetic ordering (FM or AFM) and Mn-Mn distance was also discussed for other Mn-based compounds in the past (e.g., in Ref. [19]). The shorter Mn-Mn distances result in an AFM coupling in the $Mn_3Ni_{20}P_6$ compound, while the isostructural compound $Mn_3Pd_{20}P_6$ shows ferromagnetism due to the larger Mn-Mn separation.

Spichkin and Tishin showed that the major contribution to the MC effect comes from the change in the exchange energy, which can be related to the change in the exchange parameters through the first-order magnetic phase transition for rare-earth metals (Tb, Dy, Er) and compounds ($Tb_{0.5}Dy_{0.5}$, $Gd_5Si_{1.7}Ge_{2.3}$) as well as $Fe_{0.49}Rh_{0.51}$ [20,21].

Fe_2P and its alloys, e.g., $Fe_{1-y}Mn_yP_{1-x}Si_x$, were widely investigated experimentally from a magnetocaloric point of view [2,5–7,9,10,22] and are considered to be collinear ferromagnetic materials [23–26]. These materials show a positive magnetocaloric effect when they go from the FM state to a PM state at a Curie temperature T_C typically ranging from 260 to 350 K [10]. Early on, the appearance of antiferromagnetism at ambient conditions was reported only for $FeMnP_{1-x}As_x$ [27]. Recently, however, a state with very low net magnetization has been observed for $FeMnP_{0.75}Si_{0.25}$ [28] at low temperatures. Further investigations [29] have shown the coexistence of two phases in the $FeMnP_{0.75}Si_{0.25}$ sample: phases A and B with a very distinguishable difference in the crystal structure. After the first heat treatment of the sample the phase ratio is estimated to be A/B $\approx$ 70/30 [29]. The collected magnetization data indicate a ferromagnetic ordering with $T_C = 250$ K due to the majority of phase A. After the second heat treatment of the sample the phase ratio changes to A/B $\approx$ 10/90. Magnetization data collected after the second heat treatment indicate the existence of an incommensurate antiferromagnetic ordering due to phase B with a Néel temperature $T_N \approx 150$ K and propagation vector $q_x = 0.363(1)$ measured at 16 K [29]. Neutron diffraction measurements reveal very small deviations from the nominal composition [29].

The strong coupling between crystal structure and magnetic state (FM or incommensurate AFM) is interesting on its own. However, since it is not explored if such strong local exchange striction has relevance for the performance of a magnetocaloric material, more investigations are necessary. The present study aims to identify the mechanism behind the strong local exchange striction in terms of the electronic structure of the material. Earlier electronic structure studies on the relation between the structure and magnetic configuration were based on total energy calculations [17,18]. Here we adopt a different approach to investigate the magnetostructural coupling. Namely, the magnetic exchange interactions are extracted from first-principles calculations, after which a spin-dynamics simulation is applied to obtain the final magnetic

*erna.delczeg@physics.uu.se

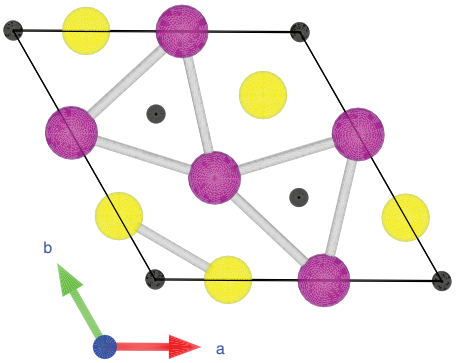

FIG. 1. (Color online) Rhombohedral building blocks of $FeMnP_{0.75}Si_{0.25}$ in the (a, b) plane. Fe-Fe (yellow balls) and Mn-Mn (purple balls) shortest-in-plane bonds are represented by gray rods. P/Si atoms (small black balls) are randomly distributed on the 2c and 1b positions.

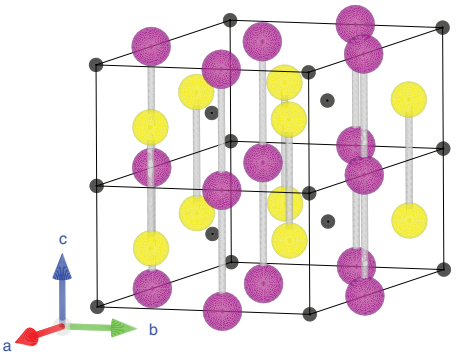

FIG. 2. (Color online) Fe-Fe (yellow balls) and Mn-Mn (purple balls) out-of-plane [along the c (z) axis] NNs of $FeMnP_{0.75}Si_{0.25}$. P/Si atoms (small black balls) are randomly distributed on the 2c and 1b positions.

configuration at finite temperatures. Using these theoretical predictions, we discuss the available experimental data [29]. The rest of this paper is organized as follows. Section II gives an overview of the crystal structures and the applied computational methods. Results and discussion are given in Sec. III. Finally, the paper concludes with a brief summary of the reported results in Sec. IV.

II. CRYSTAL STRUCTURE AND NUMERICAL DETAILS

The experimentally reported A and B phases of $FeMnP_{0.75}Si_{0.25}$ alloys both crystallize in the hexagonal Fe_2P crystal structure (space group $P\bar{6}2m$, 189) [29]. The unit cell of Fe_2P contains six Fe atoms situated in the threefold-degenerate 3f (tetrahedral) and 3g (pyramidal) Wyckoff positions, and the three P atoms are accommodated on the 2c and 1b positions. The basal (a, b) plane of the rhombohedral subcell is presented in Fig. 1. Experimentally, it is known that Fe mainly occupies the 3f tetrahedral position with the (x_1, 0, 0) coordinates, while Mn favors the 3g pyramidal position with the (x_2, 0, 1/2) coordinates. Deviations from the site occupancy are less than 6% [29]. Fe atoms are surrounded by four P/Si atoms, while Mn has five P/Si atoms as neighbors. Alternating Fe and Mn layers along the c crystallographic axis are shown in Fig. 2. There is no experimentally reported Si site preference in $FeMnP_{0.75}Si_{0.25}$. Significant differences between the lattice parameters of phases A and B are given in Table I.

The ground-state electronic structure was modeled on the level of density functional theory (DFT) using the Green's-function-based exact muffin-tin orbitals (EMTO) method [30–33]. EMTO theory formulates an efficient way to solve the Kohn-Sham equation [34]. A full description of the EMTO theory and the corresponding method may be found in Refs. [30–33]. Within this approach the compositional disorder for the P-Si atoms was treated using the coherent potential approximation [35,36]. Here we take a perfect ordering of the Fe and Mn atoms. The effect of Fe/Mn disorder is discussed elsewhere [37].

TABLE I. Experimental lattice parameters a and c (Å), volume V (Å^3), hexagonal axial ratio c/a, and in-plane metal-metal distances d_{Fe-Fe}, d_{Mn-Mn}, and d_{Fe-Mn} (Å) for phases A and B of $FeMnP_{0.75}Si_{0.25}$.

Phase	a^{exp}	c^{exp}	V^{exp}	$(c/a)^{exp}$	d_{Fe-Fe}	d_{Mn-Mn}	d_{Fe-Mn}
A	6.163	3.304	108.66	0.536	2.753	3.241	2.709
B	5.976	3.488	107.86	0.584	2.634	3.126	2.728

The ground-state information is then used to extract the intersite exchange integrals $\mathcal{J}_{ij}$ (i and j denote Fe and Mn positions). $\mathcal{J}_{ij}$ were calculated for collinear spins within the magnetic force theorem [38]:

$$\mathcal{J}_{ij} = \frac{1}{4\pi}\,\mathrm{Im}\int_{-\infty}^{E_F} dE\, Tr_L(\Delta_i T_{ij,\uparrow}\Delta_j T_{ji,\downarrow}), \qquad (1)$$

where $\Delta_i = t_{i,\uparrow}^{-1} - t_{i,\downarrow}^{-1}$ and $t_{i,s}$ and $T_{ij,s}$ ($s = \uparrow, \downarrow$) are the spin-projected single-site scattering matrices and the matrices of the scattering path operator, respectively. Note that the trace was taken in angular momentum space, $L = (\ell,m)$, and we omitted labeling explicitly the energy dependence of the occurring scattering matrices. Recently, a noncollinear generalization of Eq. (1) was proposed [39], but that generalization was not pursued in this work.

The one-electron equations were solved within the scalar-relativistic and soft-core approximations. The Green's function was calculated for 20 complex energy points distributed exponentially on an ellipsoidal contour including states within 1.5 Ry below the Fermi level. The s, p, d, and f orbitals were included in the basis set, and an $l^h_{max} = 10$ cutoff was used in the one-center expansion of the full charge density. The electrostatic correction to the single-site coherent potential approximation was described using the screened impurity model [40] with a screening parameter of 0.902. The Fe/Mn 3d and 4s and the P/Si 2s and 2p electrons were treated as valence electrons, respectively. To obtain the accuracy needed for the calculations, a $21 \times 21 \times 27$ k-point mesh was used within the Monkhorst-Pack scheme [41]. This gives more than 3900 k points in the irreducible wedge of the Brillouin zone. The self-consistent EMTO calculations were performed within the local-spin-density approximation (LSDA) [42], which gave a

good description of the magnetic properties of Fe_2P and related systems [23,25,26,43–46].

In order to investigate the importance of the many-body effects in $FeMnP_{0.75}Si_{0.25}$, we have performed a set of calculations with special treatment of the localized 3*d* electrons of Fe and Mn. For these electronic states an effective single-impurity problem is solved by means of the dynamical mean-field theory (DMFT) equations [47]. Such treatment enables us to capture all the local correlation effects that the defined electrons are exposed to. The present technique, called DFT+DMFT, is the state-of-the-art method for modeling the electronic structure from first principles [48]. We have used a charge self-consistent (CSC) version of this method, as incorporated in the full-potential LMTO code RSPT [49]. As a DMFT solver we adapted the spin-polarized T-matrix and fluctuation exchange (SPTF) method [50]. It operates in a weak-correlation limit and was successfully applied to the series of bulk transition metals, their surfaces, and alloys [51,52]. Since transition-metal-transition-metal distances in $FeMnP_{0.75}Si_{0.25}$ are rather close to the bulk values of the corresponding 3*d* metals, we anticipate a similar degree of electron localization here. In our study we have used a version of the solver in which the Feynman diagrams are calculated using partially renormalized (i.e., "dressed") Green's functions G_{HF}, where HF stands for the Hartree-Fock treatment. Such a computational setup shows a systematic improvement in the description of the magnetic properties of various systems [53].

The localized 3*d* orbitals to be treated in DMFT were defined by performing a projection onto a muffin-tin (MT) sphere around the chosen atom (so-called MT-head projection). The parameter of the screened Coulomb interaction U was set to 2.3 and 3.0 eV for Fe and Mn, respectively. Intrasite exchange was chosen to be 0.9 eV for both atomic species. These values are adapted from prior studies of bulk transition metals, which provided a fair agreement with existing experimental data [51,54,55]. The static part of the self-energy was used as a double-counting correction of the single-electron states.

The collinear EMTO calculations were augmented by noncollinear spin-spiral total-energy calculations using two different implementations. Most of the noncollinear calculations were performed using the linear muffin-tin orbital method in the atomic sphere approximation, but the results were carefully validated against the more accurate but slower full potential linear augmented-plane-wave method (LAPW) as implemented in the ELK software package [56]. We found only minor differences between the two methods regarding magnetic moments and ordering. In both softwares we employ the virtual crystal approximation (VCA) for the treatment of the compositional disorder of P and Si. These softwares allow for ground-state magnetic structure determination by minimizing the torque on each atom, i.e., zero-temperature spin dynamics, as well as superimposing of a spin-spiral propagation vector employing the generalized Bloch theorem simulating helical magnetic structures [57].

The magnetic dynamical properties of the $FeMnP_{0.75}Si_{0.25}$ system were investigated using an atomistic spin dynamics approach recently implemented in Ref. [58] at a temperature $T = 16$ K. The equation of motion of the classical atomistic spins $\mathbf{s}_i$ at finite temperature is governed by Langevin dynamics via a stochastic differential equation, normally referred to as the atomistic Landau-Lifshitz-Gilbert (LLG) equations, which can be written in the form

$$\frac{\partial \mathbf{s}_i}{\partial t} = -\frac{\gamma}{1+\alpha_i^2}\mathbf{s}_i \times [\mathbf{B}_i + \mathbf{b}_i(t)] - \frac{\gamma\alpha_i}{s(1+\alpha_i^2)}\mathbf{s}_i \times \mathbf{s}_i \times [\mathbf{B}_i + \mathbf{b}_i(t)], \quad (2)$$

where γ is the gyromagnetic ratio and α_i denotes a dimensionless site-resolved damping parameter which accounts for the energy dissipation that eventually brings the system into a thermal equilibrium. The effective field in this equation is calculated as $\mathbf{B}_i = -\partial\mathcal{H}/\partial\mathbf{s}_i$, where $\mathcal{H}$ represents an effective Heisenberg Hamiltonian given by

$$\mathcal{H} = -\sum_{\langle ij\rangle} \mathcal{J}_{ij}\mathbf{s}_i \cdot \mathbf{s}_j. \quad (3)$$

The exchange parameters $\mathcal{J}_{ij}$ have been taken from the EMTO method as given by Eq. (1). The temperature fluctuations T are considered through a random Gaussian-shaped field $\mathbf{b}_i(t)$ with the following stochastic properties:

$$\langle b_{i,\mu}(t)\rangle = 0,$$
$$\langle b_{i,\mu}(t) b_{j,\nu}(t')\rangle = \frac{2\alpha_i k_B T \delta_{ij}\delta_{\mu\nu}\delta(t-t')}{s(1+\alpha_i)^2\gamma}, \quad (4)$$

where i and j are atomic sites and μ and ν represent the Cartesian coordinates of the stochastic field. After solving the LLG equations, we have direct access to the dynamics of the atomic magnetic moments $\mathbf{s}_i(t)$.

III. RESULTS

A. Electronic structure and magnetic moments of ferromagnetic $FeMnP_{0.75}Si_{0.25}$

The electronic structure and magnetic properties discussed here were derived for the ferromagnetic $FeMnP_{0.75}Si_{0.25}$ in phase A. Spin-, site-, and orbital-projected densities of states (DOSs) presented in Fig. 3 have been obtained using the EMTO method in combination with the coherent potential approximation for the P sites. Due to the fact that in the Green's function formalism the DOS is calculated on the energy contour, the DOS plots do not show sharp peaks but contain all the features typical for Fe_2P-type systems [23,45].

$FeMnP_{0.75}Si_{0.25}$ shows metallic behavior in both spin-up and spin-down channels. The low-energy region of the total DOS (from -1 to -0.6 Ry) originates from the P and Si *s* states. The observed small shift between the spin-down and spin-up channels of P/Si is a result of a small exchange splitting induced by Fe and Mn and is consistent with the small magnetic moment of P and Si (see Table II). The P/Si *p* states contribute to the middle-energy DOS from -0.6 to -0.2 Ry. Fe and Mn 3*d* states give the main contribution to the DOS between -0.2 Ry and the Fermi level (0 Ry). A clear hybridization can be observed between the Fe/Mn 3*d* states and P/Si *p* states. Phosphorus hybridizes more strongly than Si. More 3*d* spin-down states are occupied for Fe than for Mn, in agreement with the larger number of valence electrons for Fe. The spin-up channels for Fe and Mn look very similar. The *f* orbitals do not contribute to the DOS.

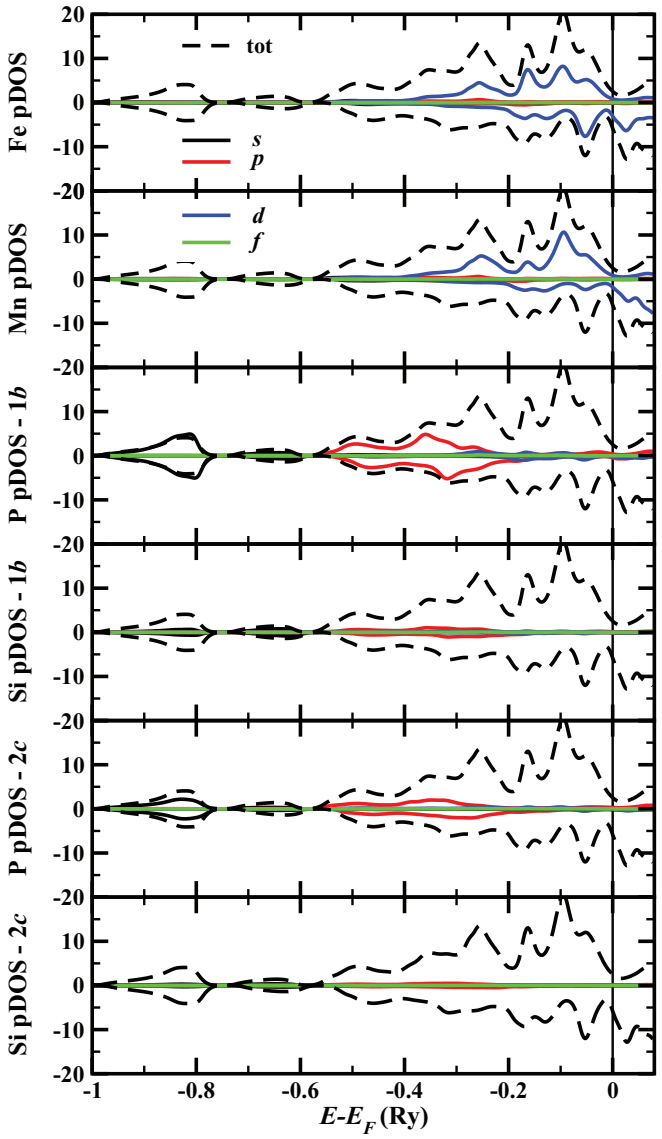

FIG. 3. (Color online) Site-, spin-, and orbital-projected DOSs (arbitrary units per atom) of ferromagnetic $FeMnP_{0.75}Si_{0.25}$. The dashed black line stands for the total DOS, the orbital projected s, p, d, and f DOSs are represented by black, red, blue, and green solid lines, respectively.

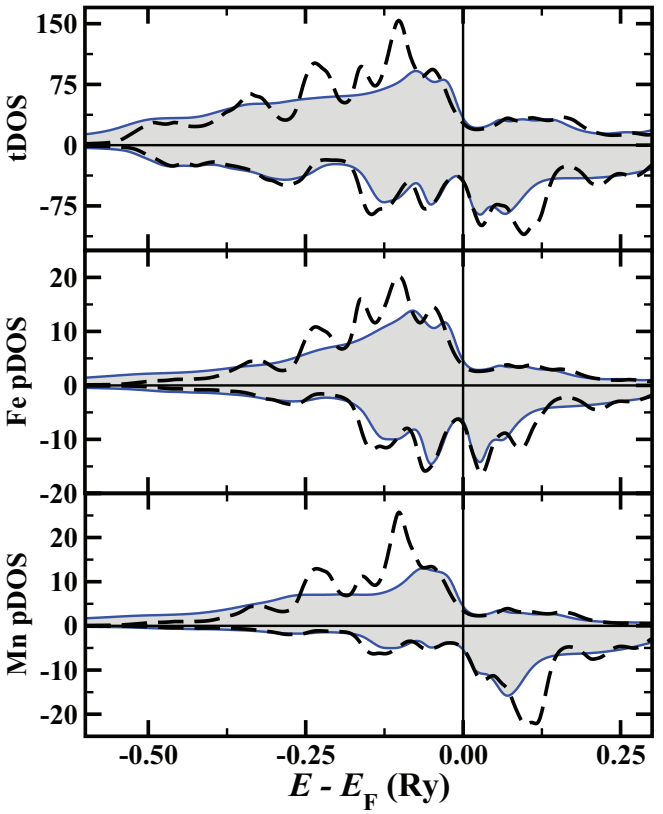

FIG. 4. (Color online) Total and site-projected DOSs (arbitrary units per unit cell) of ferromagnetic $FeMnP_{0.75}Si_{0.25}$ calculated with RSPT. Solid lines represent the LSDA+DMFT results; dashed lines correspond to the LSDA. Disorder in P and Si is modeled using VCA. Site-projected DOS is computed by performing an integration within the muffin-tin spheres with radii of 2.1 a.u. The Fermi level is set to zero energy.

In order to quantify the importance of correlation effects, we performed the DMFT-augmented calculations for the 3*d* states of Fe and Mn ions in $FeMnP_{0.75}Si_{0.25}$. The computed DOSs of ferromagnetic $FeMnP_{0.75}Si_{0.25}$ obtained from LSDA and LSDA+DMFT calculations are depicted in Fig. 4. In general, it is seen that the many-body effects are more significant for the majority-spin electrons. This is in line with the previous results [51], and the explanation can be found in Ref. [59]. In a strong ferromagnet (i.e., a system where the majority-spin

TABLE II. Experimental and theoretical site-projected magnetic moments in units of μ_B. Theoretical magnetic moments are calculated within DFT and DMFT framework.

Method	Phase	M_{Fe}	M_{Mn}	M_P/M_{Si} on 1*b*	M_P/M_{Si} on 2*c*	M_{total}/f.u.
Experiment	A	2.1	2.8			4.9
	B	2.2	2.0			≈0
EMTO-LSDA	A	1.62	2.81	−0.14/ − 0.13	−0.10/ − 0.09	4.30
	B	1.33	2.70	−0.15/ − 0.14	−0.10/ − 0.09	
	cAFM	0	2.55	0/0	0/0	0
RSPT-LSDA	A	1.46	2.80	−0.09	−0.05	4.30
	B	1.18	2.75	−0.08	−0.05	
RSPT-LSDA+DMFT	A	1.42	2.78	−0.09	−0.05	4.25
	B	1.12	2.64	−0.08	−0.05	

band is filled), an excitation of a spin-up electron ubiquitously involves spin-flip transitions, which cost more energy than electron-hole excitations in the same spin channel (which is permitted for the spin-down electrons). As a result of the correlation effects, the DOS in the spin-up channel becomes more spread in energy, and its features become less pronounced compared to the LSDA results.

The magnetic moments obtained through DFT and DFT+DMFT schemes for collinear ferromagnetic $FeMnP_{0.75}Si_{0.25}$ in both phases A and B are listed in Table II. The magnetic moments calculated within the DFT+DMFT framework are projected onto MT spheres, and the total value takes into account the interstitial contribution. The theoretically obtained magnetic moments for Mn occupying the $3g$ position are in good agreement with the experimental data for phase A. The discrepancy observed for the other local moments is discussed later in Sec. III C. We find very small induced magnetic moments on P and Si. They couple antiparallel to the Fe and Mn moments. The magnetization density presented in Fig. 5 is taken in different cutting planes of the crystal structure for ferromagnetic $FeMnP_{0.75}Si_{0.25}$ and shows a strong localization of the magnetization around Fe and Mn atoms. Similar localization was found earlier for Fe_2P [60].

A comparison between DFT and DFT+DMFT results reveals that correlation has no significant effect on the electronic structure and magnetic properties of $FeMnP_{0.75}Si_{0.25}$. The magnetic moments and number of electrons obtained by the two theoretical approaches are very similar; therefore further analysis of the magnetic exchange couplings and noncollinearity is performed within the DFT framework.

B. Collinear configurations

Two sets of exchange interactions $\mathcal{J}_{ij}$ have been calculated in a collinear ferromagnetic configuration at 0 K for $FeMnP_{0.75}Si_{0.25}$. The first set is generated using the experimental crystal structure for phase A, and the other one is generated using the experimental crystallographic data for phase B. Both crystal structures contain six magnetic atoms (three Fe and three Mn atoms) per unit cell, which represent six different sublattices. Fe atoms located at the $3f$ positions will be labeled 1–3, and Mn atoms located at the $3g$ positions will be labeled 4–6. Due to symmetry relations, we can reduce the total number of $\mathcal{J}_{ij}$ to six independent exchange parameters as follows:

$$\mathcal{J}_{11} = \mathcal{J}_{22} = \mathcal{J}_{33} \equiv \mathbf{J}_{(\mathrm{Fe-Fe})_1},$$
$$\mathcal{J}_{12} = \mathcal{J}_{13} = \mathcal{J}_{23} \equiv \mathbf{J}_{(\mathrm{Fe-Fe})_2},$$
$$\mathcal{J}_{14} = \mathcal{J}_{25} = \mathcal{J}_{36} \equiv \mathbf{J}_{(\mathrm{Fe-Mn})_1},$$
$$\mathcal{J}_{15} = \mathcal{J}_{16} = \mathcal{J}_{24} = \mathcal{J}_{26} = \mathcal{J}_{34} = \mathcal{J}_{35} \equiv \mathbf{J}_{(\mathrm{Fe-Mn})_2},$$
$$\mathcal{J}_{44} = \mathcal{J}_{55} = \mathcal{J}_{66} \equiv \mathbf{J}_{(\mathrm{Mn-Mn})_1},$$
$$\mathcal{J}_{45} = \mathcal{J}_{46} = \mathcal{J}_{56} \equiv \mathbf{J}_{(\mathrm{Mn-Mn})_2},$$

where we label the interactions for the groups by $\mathbf{J_{ij}}$. Note that, by definition, $\mathcal{J}_{ij} = \mathcal{J}_{ji}$. For each sublattice it is, of course, possible to have the exchange interaction as a function of the distance between atoms. This is shown in Fig. 6 for both phases A and B of $FeMnP_{0.75}Si_{0.25}$ calculated in a collinear ferromagnetic configuration.

$\mathbf{J}_{(\mathrm{Fe-Fe})_1}$, $\mathbf{J}_{(\mathrm{Fe-Mn})_1}$, and $\mathbf{J}_{(\mathrm{Mn-Mn})_1}$ interactions are dominated by the nearest-neighbor ferromagnetic exchange, which decays for longer range. The other three interactions, $\mathbf{J}_{(\mathrm{Fe-Fe})_2}$, $\mathbf{J}_{(\mathrm{Fe-Mn})_2}$, and $\mathbf{J}_{(\mathrm{Mn-Mn})_2}$, show oscillatory behavior, which is emphasized in the insets of Fig. 6. The first- and third-NN interactions are positive, while the second-NN interaction is negative. Mixed interactions, $\mathbf{J}_{(\mathrm{Fe-Mn})_1}$ and $\mathbf{J}_{(\mathrm{Fe-Mn})_2}$, have the largest values; $\mathbf{J_{ij}}$ between Mn atoms have intermediate values, while interactions between the Fe atoms are smaller. The differences between the various groups of interactions are smaller in the case of the Mn- and Si-doped system compared to pure Fe_2P [46].

The effect of the crystal structure on the magnetic interactions of $FeMnP_{0.75}Si_{0.25}$ is clear. The first-NN interactions for $\mathbf{J}_{(\mathrm{Fe-Fe})_1}$, $\mathbf{J}_{(\mathrm{Fe-Mn})_1}$, and $\mathbf{J}_{(\mathrm{Mn-Mn})_1}$ obtained for phase B are smaller than those for phase A. The rest of these interactions are small. This implies that the FM coupling in phase B is weaker than that in phase A. The weakening of the ferromagnetic coupling for phase B can be related to the shortening of the Fe-Fe separation. The Fe-Fe distance in phase B is 4.5% smaller than that in the phase A, allowing for a larger overlap between the wave functions that belong to different sites. Similar results have been found for $FeMnP_{0.7}As_{0.3}$ [27]. The stabilization of the FM magnetic structure is due to the localization of the Fe moments induced by the larger Fe-Fe distance in the ferromagnetic phase. This is, in general,

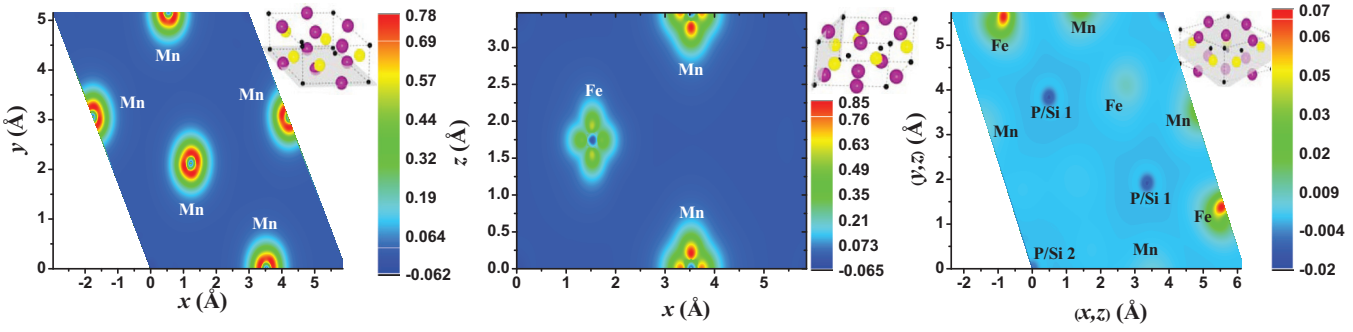

FIG. 5. (Color online) Magnetization density of ferromagnetic $FeMnP_{0.75}Si_{0.25}$ calculated at 0 K. The magnetization density in the left, middle and right panels is taken in the (0,0,1), (0,−1,0), and (−1,−1,2) planes, respectively. The cutting planes are shown in the top right corner of each panel.

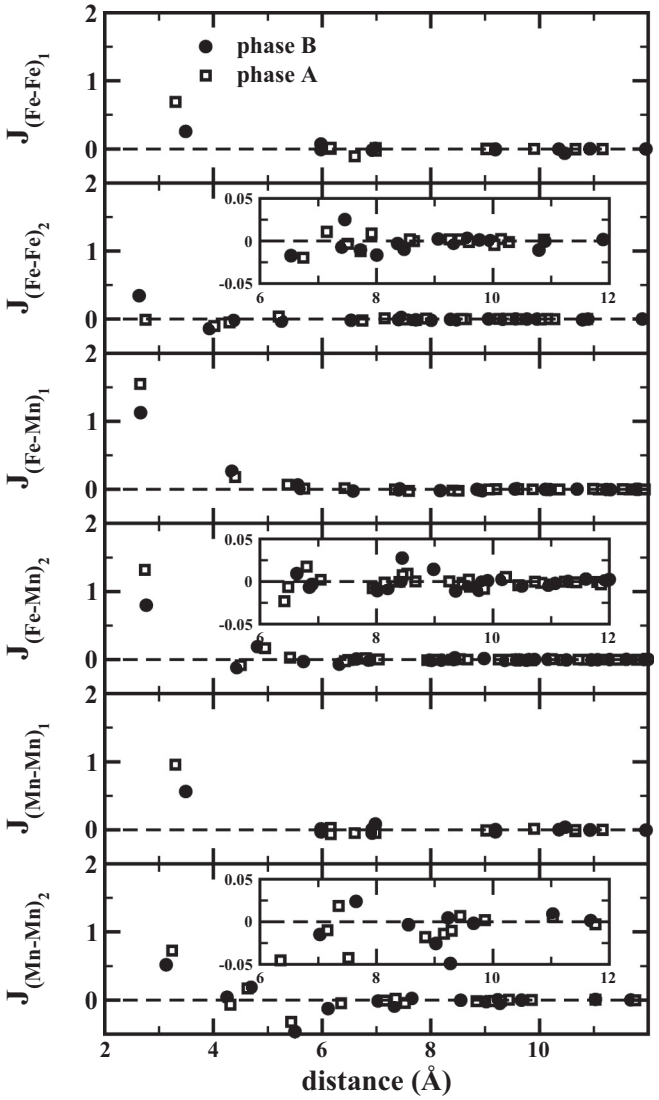

FIG. 6. Calculated Fe-Fe, Fe-Mn, and Mn-Mn exchange interactions (mRy) for phase A (open squares) and phase B (solid circles) of $FeMnP_{0.75}Si_{0.25}$ as a function of distance (Å). The insets show the oscillations at higher distances.

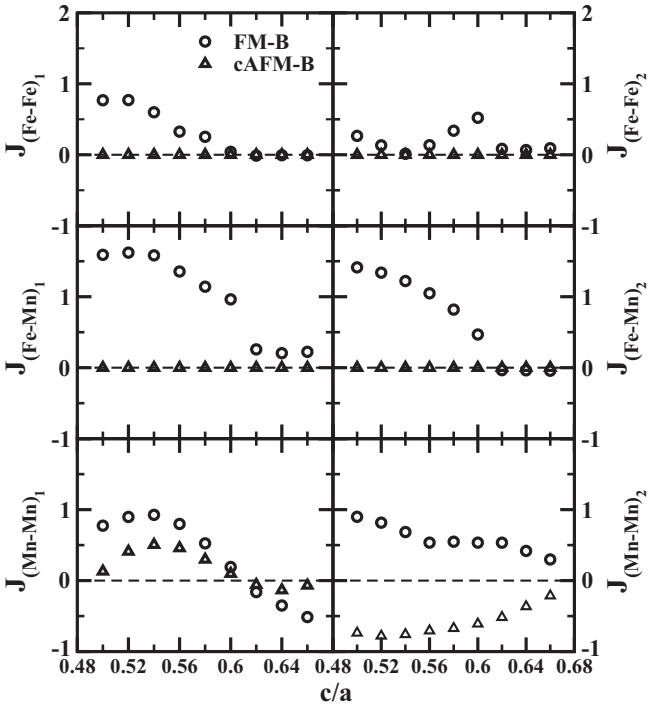

FIG. 7. First-nearest-neighbor interactions of different groups of $\mathbf{J_{ij}}$ of phase B as a function of the c/a ratio for FM-B (open circles) and cAFM-B (open triangles) configurations. The interactions $\mathbf{J_{ij}}$ are sorted into symmetry-related groups as explained in the text. See the main text for the description of the FM-B and cAFM-B configurations. Positive $\mathbf{J_{ij}}$ corresponds to the FM ground state.

accompanied by a narrowing of the Fe partial DOS, and according to Ref. [61], this leads to little overlap between spin-up and spin-down bands, which strengthens ferromagnetism over noncollinear or antiferromagnetic states.

The other three types of interactions of phase B have a smaller magnitude, in both the positive and negative regions. $\mathbf{J}_{(Fe-Fe)_2}$ is small compared to the other two interactions, i.e., $\mathbf{J}_{(Fe-Mn)_2}$ and $\mathbf{J}_{(Mn-Mn)_2}$. Also, $\mathbf{J}_{(Fe-Mn)_2}$ and $\mathbf{J}_{(Mn-Mn)_2}$ reach larger absolute values in the negative region for phase B. Besides the weaker FM coupling, a strengthening of the AFM coupling appears for phase B. Here the change in the magnetic behavior may be related to the large change in the Mn-Mn separation. The mean Mn-Mn distance is 3.7% smaller for phase B than for phase A, which is expected to lead to an increased tendency for AFM interactions.

A closer analysis of the NN interactions was done using the c/a ratio as the most relevant materials parameter. Different groups of NN $\mathbf{J_{ij}}$ are calculated for different c/a ratios while keeping the value of the internal parameters and volume fixed to the experimental values of phase B for two magnetic configurations: a collinear FM ordering (labeled FM-B) and a simple collinear commensurate ($q_z = 0.5$) AFM structure (labeled cAFM-B). The results are presented in Fig. 7, where positive $\mathbf{J_{ij}}$ indicates the stability of the FM state. The NN $\mathbf{J}_{(Fe-Fe)_1}$ and $\mathbf{J}_{(Mn-Mn)_1}$ interactions correspond to the closest out-of-plane interactions along the c crystallographic axis as illustrated in Fig. 2. The NN in-plane $\mathbf{J}_{(Fe-Fe)_2}$ and $\mathbf{J}_{(Mn-Mn)_2}$ interactions are presented in Fig. 1. Due to the crystal structure, the NN $\mathbf{J}_{(Fe-Mn)_1}$ and $\mathbf{J}_{(Fe-Mn)_2}$ interactions have both in-plane and out-of-plane contributions. One can see from Fig. 7 that most of the interactions calculated for the collinear ferromagnetic case FM-B are positive for the whole range of c/a ratios, implying a FM coupling. Only $\mathbf{J}_{(Mn-Mn)_1}$ becomes negative for c/a values higher than that of the experimental value of phase B. However, the situation changes for the simple collinear commensurate antiferromagnetic cAFM-B case. Fe moments then disappear for all values of the c/a ratio, similar to what was discussed in Refs. [46,62,63]; therefore $\mathbf{J}_{(Fe-Fe)_1}$, $\mathbf{J}_{(Fe-Fe)_2}$, $\mathbf{J}_{(Fe-Mn)_1}$, and $\mathbf{J}_{(Fe-Mn)_2}$ become zero. The Mn moments do not disappear, however, and have a value a bit smaller ($2.5\mu_B$ at the experimental c/a ratio of phase B) than that of Mn moments for a ferromagnetic configuration of phase B at the experimental c/a ratio (see Table II). $\mathbf{J}_{(Mn-Mn)_1}$ is positive for lower c/a ratios and changes sign at high c/a ratios above and close to the experimental c/a value of phase

B. $\mathbf{J}_{(\mathrm{Mn-Mn})_2}$ is negative in the cAFM-B configuration for the whole c/a range.

To conclude this section, Figs. 6 and 7 show that both crystal structure and magnetic structure critically influence the exchange interactions between all atoms of this material and are decisive if finite Fe moments are found in this material.

C. Noncollinear configurations

The existence of a helical magnetic structure for phase B has been further explored with noncollinear spin-spiral total-energy calculations. Without allowing for spin spirals these LMTO-based total energies show that at 0 K the ground-state magnetic structure has a ferromagnetic alignment of the Fe and Mn moments for the structural parameters of phase B. The Fe moments are around $1.5\mu_B$ and $2.6\mu_B$ for Mn, in good agreement with the EMTO and RSPT results (see Table II), but with a marked deviation of the reported experimental magnetic moment of the noncollinear configuration of phase B (Table II). We note, however, that the experimental analysis of phase B was not perfect in regard to the size of the magnetic moments, and hence the disagreement between experimental and theoretical moments for the noncollinear phase B may not to be too alarming. By constraining the magnetic structure in different noncollinear orientations among the moments in the calculations, we find that there are many magnetic configurations that are close in energy compared to the ground-state ferromagnetic configuration. This indicates that the system might form more complicated magnetic structures for a slightly modified composition and/or at elevated temperatures. Since the Fe moments are induced from the local magnetic field from the Mn moments and therefore are very soft, the Fe moments become small or vanish when the internal orientation of the Mn atoms form configurations other than ferromagnetic. For instance, the Fe local moment decreases by a factor of 2 (from $1.5\mu_B$ to around $0.8\mu_B$) when the angle between the Mn moments is 180° and vanishes completely when the Fe and Mn moments are perpendicular to each other.

Allowing for a spin spiral propagating along the b axis simulates a noncollinear helical magnetic configuration. However, for any finite wave vector of the spin spiral the total energy is higher compared to ferromagnetic alignment. At the zone boundary, which corresponds to antiferromagnetic alignment, the total energy is around 4 mRy/f.u. higher than that of the FM structure.

D. Magnetodynamical properties

The results from all the calculations that we have performed for $FeMnP_{0.75}Si_{0.25}$ (ferromagnetic, antiferromagnetic, and noncollinear) show overall that the size of the Fe moment depends on the type of magnetic configuration, similar to Fe_2P [62,63] and Si-doped Fe_2P [62]. This becomes rather extreme in certain situations, as was pointed out in Refs. [62,63], where the Fe1 moment on the $3f$ site can disappear when their coupling to the Fe2 moments on the $3g$ sites is purely antiferromagnetic. However, for smaller angles between Fe and Mn moments, they maintain the size they have in a ferromagnetic configuration, which indicates that a Heisenberg description is applicable, at least within some limits. We have investigated how far such a picture can be used to explain the magnetic properties of $FeMnP_{0.75}Si_{0.25}$ and have therefore combined a Heisenberg Hamiltonian with an approach of atomistic spin dynamics. We have hence evolved in time the atomic magnetic moments of both phase A and phase B initial magnetic configurations with the exchange parameters given by the EMTO method at $T = 16$ K, the temperature at which measurements were conducted. The predicted magnetic ground state is FM for the exchange constants of phase A, while the system evolves into a helical spin structure for the exchange couplings of phase B. We calculated the Fourier transform of the static correlation function with the aim of determining the q vector of the spin spiral. The ASD method predicts a value for the q vector of (0.25,0,0) along the propagation direction, as shown in Fig. 8. The angle between the Fe and Mn moments is about 14°, and the moments lie almost exclusively in the (a,b) plane. The predicted q vector is in rather good agreement with the reported experimental results (0.363,0,0) [29]. Unfortunately, the complete magnetic structure of $FeMnP_{0.75}Si_{0.25}$ was not resolved in Ref. [29], so a more detailed comparison between experiment and theory is not possible for phase B, e.g., with regard to the size of the magnetic moments.

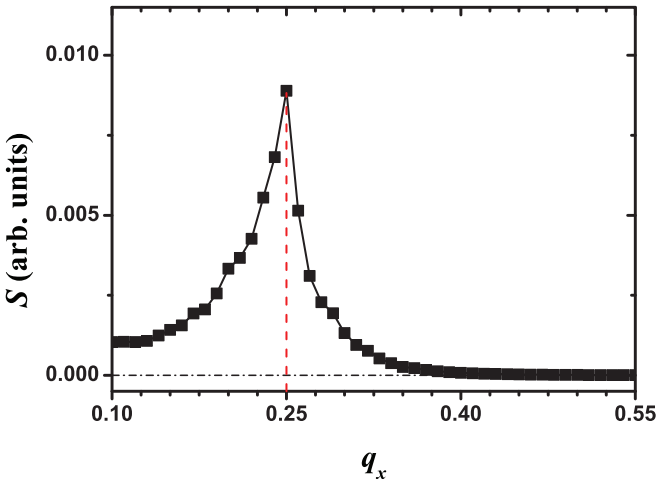

FIG. 8. (Color online) Ground-state helical configuration predicted by ASD simulations for phase B. The Fourier transform of the static correlation function is plotted vs the q_x vector.

E. Discussion

The total energies of the FM-B and cAFM-B configurations calculated using the internal parameters and volume of phase B of $FeMnP_{0.75}Si_{0.25}$ are plotted in Fig. 9 as a function of the c/a ratio and a axis. The collinear ferromagnetic configuration FM-B has its total energy minimum at $c/a = 0.534$ and $a = 6.166$ Å, values close to the experimental value of phase A given in Table I. The 0.9 mRy energy difference between the energy minima of ferromagnetic phase B and phase A is due to the difference in internal parameters between phases A and B. The energy minimum for the cAFM-B configuration is at $c/a = 0.589$ and $a = 5.963$ Å, close to the experimental value for phase B (see Table I), indicating that even a simple antiferromagnetic configuration prefers higher c/a ratios.

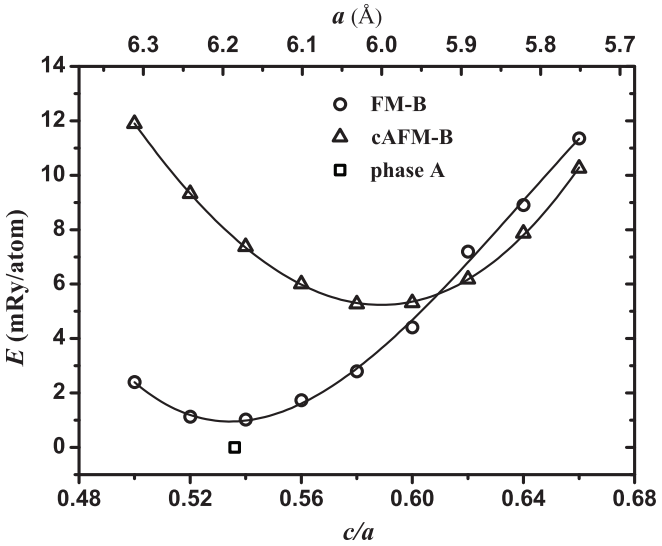

FIG. 9. Total energies E (mRy/atom) as a function of the c/a ratio and a axis for FM-B (open circles) and cAFM-B (open triangles) configurations of phase B of $FeMnP_{0.75}Si_{0.25}$. Total energies are expressed with respect to the total energy of phase A (open squares) of $FeMnP_{0.75}Si_{0.25}$.

The total-energy minimum for the cAFM-B configuration is 4.3 mRy higher than that of the FM-B configuration. However, for higher c/a ratios the cAFM-B configuration becomes lower in energy than the FM-B configuration. The common tangent of the two E vs c/a ratio curves indicates the coexistence of cAFM-B and FM-B phases between c/a ratios of approximately 0.58 and 0.63. The magnetic phase change seems to be accessible, applying a strain of ≈15 GPa to the FM-B phase along the a and b directions.

DOS analysis can give deeper insight into the relative stability of different phases. Figure 10 shows DOS for different crystallographic and magnetic phases of $FeMnP_{0.75}Si_{0.25}$. The spin-down channel is not significantly affected by the

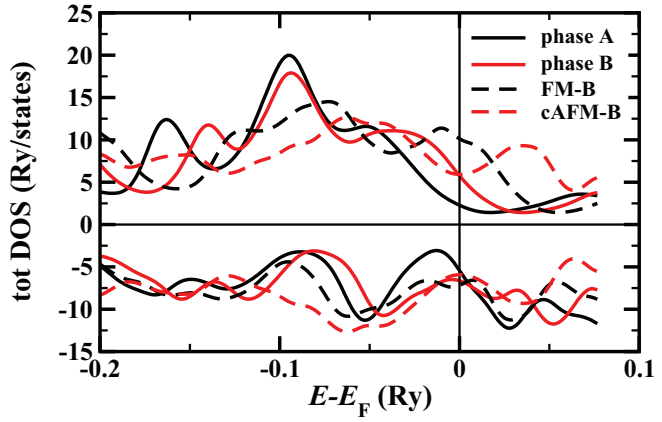

FIG. 10. (Color online) Total DOS for phase A (solid red line) and phase B (solid black line) of $FeMnP_{0.75}Si_{0.25}$ at the experimental c/a ratio and for the FM-B (red dashed line) and cAFM (black dashed line) configurations of $FeMnP_{0.75}Si_{0.25}$ at $c/a = 0.62$. See the main text for the description of the FM-B and cAFM-B configurations.

different crystal structures and magnetic configurations of $FeMnP_{0.75}Si_{0.25}$. However, there are major changes in the spin-up channel. Phase A possesses the lowest DOS at the Fermi level in the spin-up channel $\mathcal{N}(E_F)^{\uparrow}$, indicating that this is the stable structure and magnetic configuration at 0 K, in agreement with the total-energy results. Increasing the c/a ratio for phase A, one can get phase B in a ferromagnetic configuration, which has a higher $\mathcal{N}(E_F)^{\uparrow}$, indicating the relative instability of the structure and magnetic configuration. As the c/a ratio is further increased up to 0.62 (FM-B), a stronger destabilization is observed. The crystal structure with a high c/a ratio of 0.62 in the collinear commensurate antiferromagnetic configuration cAFM-B has lower $\mathcal{N}(E_F)^{\uparrow}$ than FM-B, indicating that this material prefers an antiparallel alignment for the magnetic moments with a high c/a ratio.

IV. CONCLUSION

We show that a detailed analysis of the magnetic exchange interactions as a function of structure and magnetic configuration of $FeMnP_{0.75}Si_{0.25}$ in combination with spin-dynamic simulation leads to agreement with experimental results in that ferromagnetic and noncollinear configurations compete and depend crucially on crystalline structure and also must possess a strong temperature dependence. We also find many competing energy minima at drastically different magnetic configurations. We also find, for phase B, the appearance of a helical spin-spiral magnetic structure at finite temperature. The q vector of the helical spin-spiral magnetic structure is in satisfactory agreement with the experimental findings. In our calculations we find Mn moments that agree with observations of the ferromagnetic phase, whereas the Fe moment is smaller than that in experiments. Possibly, this can be explained by the many competing magnetic configurations of this material. As mentioned, the lack of firm experimental information about the magnetic moments of the noncollinear phase excludes a relevant comparison between experimental and magnetic moments for this phase.

We find that the decrease in the Mn-Mn and Fe-Fe shortest interatomic distances leads to a destabilization of the FM coupling. Out-of-plane Mn-Mn exchange interactions become negative with the shortening of the interatomic distances along the c axis, implying an AFM coupling for the NN Mn-Mn interactions. The appearance of the helical magnetic structure of $FeMnP_{0.75}Si_{0.25}$ results from two factors: the Mn-Mn separation plays an important role like in the case of *Pnma* compounds [17,18], and the shortening of the Fe-Fe interatomic distance is also important in the destabilization of the FM coupling.

We also find that the size of the Fe moment depends critically on the magnetic configuration. In a rather extreme way, it disappears if it becomes perpendicular to the Mn moments or when Mn moments are antiferromagetically coupled to each other along the z axes. The sensitivity of the Fe moments in $FeMnP_{0.75}Si_{0.25}$ is similar to what has been suggested for Fe_2P [46,62,63], and direct confirmation by, e.g., neutron scattering experiments would be very interesting. Finally, our calculations suggest that different magnetic configurations for $FeMnP_{0.75}Si_{0.25}$ can be accessed at low temperatures when

strain is applied. A similar magnetic phase transition, e.g., from the ferromagnetic to antiferromagnetic configuration, was observed for Fe_2P under pressure [64–66].

ACKNOWLEDGMENTS

Valuable discussions with V. Höglin, M. Sahlberg, Y. Andersson, and P. Nordblad are acknowledged. The European Research Council, Swedish Research Council, Swedish Energy Agency, and the Swedish Foundation for International Cooperation in Research and Higher Education (STINT) are acknowledged for financial support. O.E. also acknowledges support from eSSCENCE, STANDUP, ERC (247062-ASD), and the KAW foundation. L.B. also acknowledges support from the Göran Gustafssons Foundation. The Hungarian Scientific Research Fund (research projects OTKA 84078 and 109570) is also acknowledged for financial support (L.V.). Calculations were performed on UPPMAX and NSC-Matter resources. E.K.D.-Cz. acknowledges discussions with A. V. Ruban. Y.O.K. expresses his gratitude to D. Iuşan for numerous valuable discussions and assistance with the calculations.

[1] V. K. Pecharsky and K. A. Gschneidner, Jr., Phys. Rev. Lett. **78**, 4494 (1997).
[2] O. Tegus, E. Brück, K. H. J. Buschow, and F. R. de Boer, Nature (London) **415**, 150 (2002); O. Tegus, E. Brück, L. Zhang, Dagula, K. H. J. Buschow, and F. R. de Boer, Phys. B (Amsterdam, Neth.) **319**, 174 (2002); R. Fruchart, Ann. Chim. (Cachan, Fr.) **7**, 563 (1982).
[3] A. Fujita, S. Fujieda, Y. Hasegawa, and K. Fukamichi, Phys. Rev. B **67**, 104416 (2003).
[4] H. Yamada and T. Goto, Phys. Rev. B **68**, 184417 (2003).
[5] E. Brück, O. Tegus, L. Zhang, X. W. Li, F. R. de Boer, and K. H. J. Buschow, J. Alloys Compd. **383**, 32 (2004).
[6] W. Dagula, O. Tegus, X. W. Li, L. Song, E. Brück, D. T. Cam Thanh, F. R. de Boer, and K. H. J. Buschow, J. Appl. Phys. **99**, 08Q105 (2006).
[7] E. Brück, O. Tegus, D. T. Cam Thanh, and K. H. J. Buschow, J. Magn. Magn. Mater. **310**, 2793 (2007).
[8] M.-H. Phan and S.-Ch. Yu, J. Magn. Magn. Mater. **308**, 325 (2007).
[9] D. T. CamThanh, E. Brück, N. T. Trung, J. C. P. Klaasse, K. H. J. Buschow, Z. Q. Ou, O. Tegus, and L. Caron, J. Appl. Phys. **103**, 07B318 (2008).
[10] N. H. Dung, Z. Q. Ou, L. Caron, L. Zhang, D. T. CamThan, G. A. de Wijs, R. A. de Groot, K. H. J. Buschow, and E. Brück, Adv. Energy Mater. **1**, 1215 (2011); N. H. Dung, L. Zhang, Z. Q. Ou, and E. Brück, Appl. Phys. Lett. **99**, 092511 (2011).
[11] M. P. Annaorazov, K. A. Asatryan, G. Myalikgulyev, S. A. Nikitin, A. M. Tishin, and A. L. Tyurin, Cryogenics **32**, 867 (1992).
[12] T. Tohei, H. Wada, and T. Kanomata, J. Appl. Phys. **94**, 1800 (2003).
[13] K. G. Sandeman, R. Daou, S. Özcan, J. H. Durrell, N. D. Mathur, and D. J. Fray, Phys. Rev. B **74**, 224436 (2006); K. Morrison, Y. Miyoshi, J. D. Moore, A. Barcza, K. G. Sandeman, A. D. Caplin, and L. F. Cohen, *ibid.* **78**, 134418 (2008); K. Morrison, J. D. Moore, K. G. Sandeman, A. D. Caplin, and L. F. Cohen, *ibid.* **79**, 134408 (2009); K. G. Sandeman, Scr. Mater. **67**, 566 (2012).
[14] A. Barcza, Z. Gercsi, K. S. Knight, and K. G. Sandeman, Phys. Rev. Lett. **104**, 247202 (2010); A. Barcza, Z. Gercsi, H. Michor, K. Suzuki, W. Kockelmann, K. S. Knight, and K. G. Sandeman, Phys. Rev. B **87**, 064410 (2013).
[15] J. B. Staunton, M. dos Santos Dias, J. Peace, Z. Gercsi, and K. G. Sandeman, Phys. Rev B **87**, 060404(R) (2013); J. B. Staunton, R. Banerjee, M. dos Santos Dias, A. Deak, and L. Szunyogh, *ibid.* **89**, 054427 (2014).
[16] F. Guillou and E. Brück, J. Appl. Phys. **114**, 143903 (2013).
[17] Z. Gercsi and K. G. Sandeman, Phys. Rev. B **81**, 224426 (2010).
[18] Z. Gercsi, K. Hono, and K. G. Sandeman, Phys. Rev. B **83**, 174403 (2011).
[19] T. Eriksson, M. Vennström, S. Ronneteg, Y. Andersson, and P. Nordblad, J. Magn. Magn. Mater. **308**, 203 (2007).
[20] Y. I. Spichkin and A. M. Tishin, J. Alloys Compd. **403**, 38 (2005).
[21] A. M. Tishin and Y. I. Spichkin, Int. J. Refrig. **37**, 223 (2014).
[22] X. F. Miao, L. Caron, P. Roy, N. H. Dung, L. Zhang, W. A. Kockelmann, R. A. deGroot, N. H. van Dijk, and E. Brück, Phys. Rev. B **89**, 174429 (2014).
[23] X. B. Liu and Z. Altounian, J. Appl. Phys. **105**, 07A902 (2009).
[24] H. Fujii, T. Hōkabe, T. Kamigaichi, and T. Okamato, J. Phys. Soc. Jap. **43**, 41 (1977).
[25] S. Ishida, S. Asano, and J. Ishida, J. Phys. F **17**, 475 (1987).
[26] O. Eriksson, J. Sjöström, B. Johansson, L. Häggström, and H. L. Skriver, J. Magn. Magn. Mater. **74**, 347 (1988).
[27] M. Bacmann, J. L. Soubeyroux, R. Barett, D. Fruchart, R. Zach, S. Niziol, and R. Fruchart, J. Magn. Magn. Mater. **134**, 59 (1994).
[28] M. Hudl, P. Nordblad, T. Björkman, O. Eriksson, L. Häggström, M. Sahlberg, Y. Andersson, E.-K. Delczeg-Czirjak, and L. Vitos, Phys. Rev. B **83**, 134420 (2011).
[29] V. Höglin, M. Hudl, L. Caron, P. Beran, M. H. Sørby, P. Nordblad, Y. Andersson, and M. Sahlberg, J. Solid State Chem. **221**, 240 (2015).
[30] O. K. Andersen, O. Jepsen, and G. Krier, in *Lectures on Methods of Electronic Structure Calculation* (World Scientific, Singapore 1994), p. 63.
[31] L. Vitos, H. L. Skriver, B. Johansson, and J. Kollár, Comput. Mater. Sci. **18**, 24 (2000).
[32] L. Vitos, Phys. Rev. B **64**, 014107 (2001).
[33] L. Vitos, I. A. Abrikosov, and B. Johansson, Phys. Rev. Lett. **87**, 156401 (2001).
[34] W. Kohn and L. J. Sham, Phys. Rev. **140**, A1133 (1965).
[35] P. Soven, Phys. Rev. **156**, 809 (1967).
[36] B. L. Gyorffy, Phys. Rev. B **5**, 2382 (1972).
[37] G. Li, W. Li, S. Schönecker, X. Li, E. K. Delczeg-Czirjak, Y. O. Kvashnin, O. Eriksson, B. Johansson, and L. Vitos, Appl. Phys. Lett. (to be published).
[38] A. I. Liechtenstein, M. I. Katsnelson, and V. A. Gubanov, J. Phys. F **14**, L125 (1984).

[39] A. Szilva, M. Costa, A. Bergman, L. Szunyogh, L. Nordström, and O. Eriksson, Phys. Rev. Lett. **111**, 127204 (2013).
[40] P. A. Korzhavyi, A. V. Ruban, I. A. Abrikosov, and H. L. Skriver, Phys. Rev. B **51**, 5773 (1995).
[41] H. J. Monkhorst and J. D. Pack, Phys. Rev. B **13**, 5188 (1976).
[42] J. P. Perdew and Y. Wang, Phys. Rev. B **45**, 13244 (1992).
[43] L. Severin, L. Häggström, L. Nordström, Y. Andersson, and B. Johansson, J. Phys. Condens. Matter **7**, 185 (1995).
[44] H. Yamada and K. Terao, Phase Transitions **75**, 231 (2002).
[45] X. B. Liu and Z. Altounian, J. Magn. Magn. Mater. **321**, 2005 (2009).
[46] E. K. Delczeg-Czirjak, Z. Gercsi, L. Bergqvist, O. Eriksson, L. Szunyogh, P. Nordblad, B. Johansson, and L. Vitos, Phys. Rev. B **85**, 224435 (2012); E. K. Delczeg-Czirjak, L. Bergqvist, O. Eriksson, Z. Gercsi, P. Nordblad, L. Szunyogh, B. Johansson, and L. Vitos, *ibid.* **86**, 045126 (2012).
[47] A. Georges, G. Kotliar, W. Krauth, and M. J. Rozenberg, Rev. Mod. Phys. **68**, 13 (1996).
[48] G. Kotliar, S. Y. Savrasov, K. Haule, V. S. Oudovenko, O. Parcollet, and C. A. Marianetti, Rev. Mod. Phys. **78**, 865 (2006).
[49] O. Grånäs, I. D. Marco, P. Thunström, L. Nordström, O. Eriksson, T. Björkman, and J. Wills, Comput. Mater. Sci. **55**, 295 (2012).
[50] L. V. Pourovskii, M. I. Katsnelson, and A. I. Lichtenstein, Phys. Rev. B **72**, 115106 (2005).
[51] A. Grechnev, I. Di Marco, M. I. Katsnelson, A. I. Lichtenstein, J. Wills, and O. Eriksson, Phys. Rev. B **76**, 035107 (2007).
[52] J. Minár, J. Phys. Condens. Matter **23**, 253201 (2011).
[53] O. Grånäs, Ph.D. thesis, Uppsala University, 2012.
[54] I. Di Marco, J. Minár, J. Braun, M. I. Katsnelson, A. Grechnev, H. Ebert, A. I. Lichtenstein, and O. Eriksson, Eur. Phys. J. B **72**, 473 (2009).
[55] J. Sánchez-Barriga, J. Fink, V. Boni, I. Di Marco, J. Braun, J. Minár, A. Varykhalov, O. Rader, V. Bellini, F. Manghi, H. Ebert, M. I. Katsnelson, A. I. Lichtenstein, O. Eriksson, W. Eberhardt, and H. A. Dürr, Phys. Rev. Lett. **103**, 267203 (2009); J. Sánchez-Barriga, J. Braun, J. Minár, I. Di Marco, A. Varykhalov, O. Rader, V. Boni, V. Bellini, F. Manghi, H. Ebert, M. I. Katsnelson, A. I. Lichtenstein, O. Eriksson, W. Eberhardt, H. A. Dürr, and J. Fink, Phys. Rev. B **85**, 205109 (2012).
[56] ELK software package, http://elk.sourceforge.net/.
[57] C. Herring, *Magnetism*, edited by G. Rado and H. Suhl (Academic, New York, 1966), Vol. 4.
[58] B. Skubic, J. Hellsvik, L. Nordström, and O. Eriksson, J. Phys. Condens. Matter **20**, 315203 (2008); http://www.physics.uu.se/en/page/UppASD/.
[59] S. Monastra, F. Manghi, C. A. Rozzi, C. Arcangeli, E. Wetli, H.-J. Neff, T. Greber, and J. Osterwalder, Phys. Rev. Lett. **88**, 236402 (2002).
[60] Z. Gercsi, E. K. Delczeg-Czirjak, L. Vitos, A. S. Wills, A. Daoud-Aladine, and K. G. Sandeman, Phys. Rev. B **88**, 024417 (2013).
[61] R. Lizárraga, L. Nordström, L. Bergqvist, A. Bergman, E. Sjöstedt, P. Mohn, and O. Eriksson, Phys. Rev. Lett. **93**, 107205 (2004).
[62] E. K. Delczeg-Czirjak, L. Delczeg, M. P. J. Punkkinen, B. Johansson, O. Eriksson, and L. Vitos, Phys. Rev. B **82**, 085103 (2010).
[63] X. B. Liu, J. P. Liu, Q. Zhang, and Z. Altounian, Phys. Lett. A **377**, 731 (2013).
[64] H. Fujiwara, H. Kadomatsu, K. Tohma, H. Fujii, and T. Okamoto, J. Magn. Magn. Mater. **21**, 262 (1980); H. Kadomatsu, M. Isoda, K. Tohma, H. Fujii, T. Okamoto, and H. Fujiwara, J. Phys. Soc. Jpn. **54**, 2690 (1985).
[65] M. Abliz, Y. Uwatoko, T. Ohki, H. Fujii, and R. A. Secco, J. Phys. Soc. Jpn. **75**, 123706 (2006); H. Kobayashi, J. Umemura, X.-W. Zhan, Y. Ohishi, Y. Uwatoko, H. Fujii, and N. Sakai, *ibid.* **80**, 084719 (2011).
[66] L. Caron *et al.* (unpublished).